LETTER

Observation of Dirac monopoles in a synthetic magnetic field

M. W. Ray[1], E. Ruokokoski[2], S. Kandel[1]†, M. Möttönen[2,3] & D. S. Hall[1]

Magnetic monopoles—particles that behave as isolated north or south magnetic poles—have been the subject of speculation since the first detailed observations of magnetism several hundred years ago[1]. Numerous theoretical investigations and hitherto unsuccessful experimental searches[2] have followed Dirac's 1931 development of a theory of monopoles consistent with both quantum mechanics and the gauge invariance of the electromagnetic field[3]. The existence of even a single Dirac magnetic monopole would have far-reaching physical consequences, most famously explaining the quantization of electric charge[3,4]. Although analogues of magnetic monopoles have been found in exotic spin ices[5,6] and other systems[7–9], there has been no direct experimental observation of Dirac monopoles within a medium described by a quantum field, such as superfluid helium-3 (refs 10–13). Here we demonstrate the controlled creation[14] of Dirac monopoles in the synthetic magnetic field produced by a spinor Bose–Einstein condensate. Monopoles are identified, in both experiments and matching numerical simulations, at the termini of vortex lines within the condensate. By directly imaging such a vortex line, the presence of a monopole may be discerned from the experimental data alone. These real-space images provide conclusive and long-awaited experimental evidence of the existence of Dirac monopoles. Our result provides an unprecedented opportunity to observe and manipulate these quantum mechanical entities in a controlled environment.

Maxwell's equations refer neither to magnetic monopoles nor to the magnetic currents that arise from their motion. Although a simple symmetrization with respect to the electric and magnetic fields, respectively E and B, leads to equations that involve these magnetic charges, it also seemingly prevents their description in terms of the familiar scalar and vector potentials, respectively V and A, alone. Because the quantum mechanical Hamiltonian is expressed in terms of potentials, rather than electromagnetic fields, this modification immediately leads to serious theoretical challenges.

In a celebrated paper that combined arguments from quantum mechanics and classical electrodynamics[3], Dirac identified electromagnetic potentials consistent with the existence of magnetic monopoles. His derivation relies on the observation that in quantum mechanics the potentials V and A influence charged-particle dynamics either through the Hamiltonian or, equivalently, through modifications of the complex phase of the particle wavefunction. Armed with these equivalent perspectives, Dirac then considered the phase properties of a wavefunction pierced by a semi-infinite nodal line with non-zero phase winding. He discovered that the corresponding electromagnetic potentials yield the magnetic field of a monopole located at the endpoint of the nodal line. The vector potential in this case also exhibits a nonphysical line singularity, or 'Dirac string', that terminates at the monopole.

We experimentally create Dirac monopoles in the synthetic electromagnetic field that arises in the context of a ferromagnetic spin-1 ^{87}Rb Bose–Einstein condensate (BEC) in a tailored excited state[14]. The BEC is described by a quantum mechanical order parameter that satisfies a nonlinear Schrödinger equation, and the synthetic gauge potentials describing a north magnetic pole (Fig. 1) are generated by the spin texture. This experiment builds on studies of synthetic electric and magnetic fields, respectively E^* and B^*, in atomic BECs, which is an emerging topic of intense interest in the simulation of condensed-matter systems with ultracold atoms[15,16]. Unlike monopole experiments in spin ices[5,6], liquid crystals[7], skyrmion lattices[9] and metallic ferromagnets[8], our experiments demonstrate the essential quantum features of the monopole envisioned by Dirac[3].

Physically, the vector potential, A^*, and synthetic magnetic field, $B^* = \hbar\nabla \times A^*$, are related to the superfluid velocity, v_s, and vorticity, $\Omega = \nabla \times v_s$, respectively. (Here $\hbar$ denotes Planck's constant divided by 2π.) Our primary evidence for the existence of the monopole comes from images of the condensate density taken after the creation of these fields (Figs 2 and 3), which reveal a nodal vortex line with 4π phase winding terminating within the condensate. The images also display a three-dimensional spin structure that agrees well with the results of
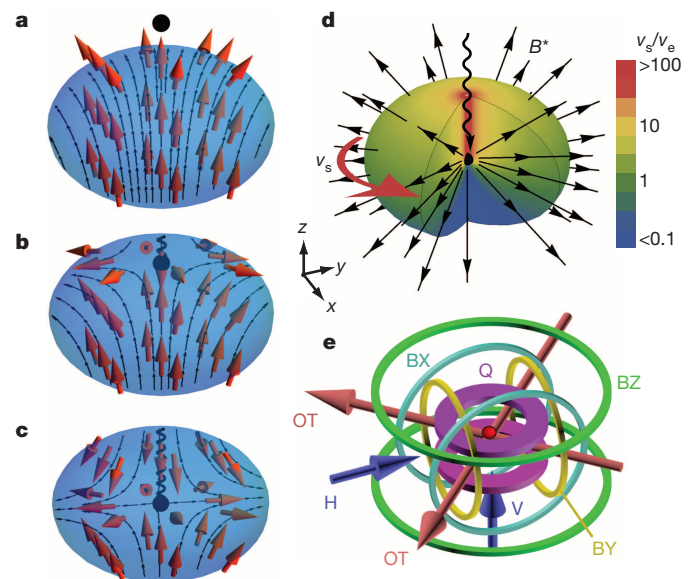
Figure 1 | Schematic representations of the monopole creation process and experimental apparatus. a–c, Theoretical spin orientation (red arrows) within the condensate when the magnetic field zero (black dot) is above (a), entering (b) and in the middle of (c) the condensate. The helix represents the singularity in the vorticity. d, Azimuthal superfluid velocity, v_s (colour scale and red arrow), scaled by equatorial velocity, v_e. Black arrows depict the synthetic magnetic field, B^*. e, Experimental set-up showing magnetic quadrupole (Q) and bias field (BX, BY and BZ) coils. Red arrows (OT) show beam paths of the optical dipole trap, and blue arrows indicate horizontal (H) and vertical (V) imaging axes. Gravity points in the $-z$ direction.

[1]Department of Physics, Amherst College, Amherst, Massachusetts 01002–5000, USA. [2]QCD Labs, COMP Centre of Excellence, Department of Applied Physics, Aalto University, PO Box 13500, 00076 Aalto, Finland. [3]Low Temperature Laboratory (OVLL), Aalto University, PO Box 13500, 00076 Aalto, Finland. †Present address: City of Hope National Medical Center, 1500 East Duarte Road, Duarte, California 91010, USA.
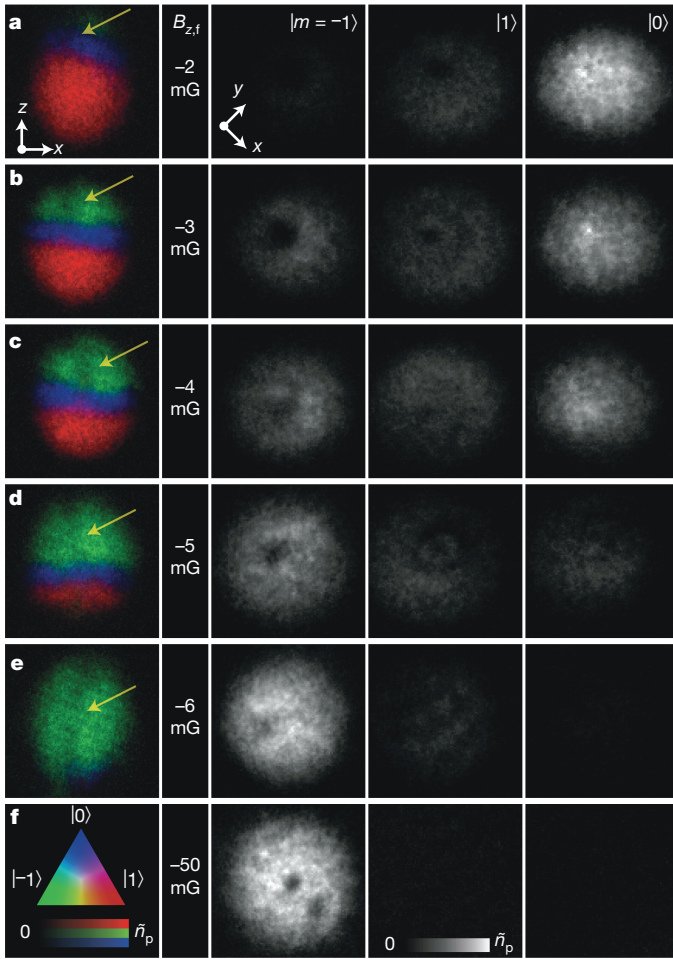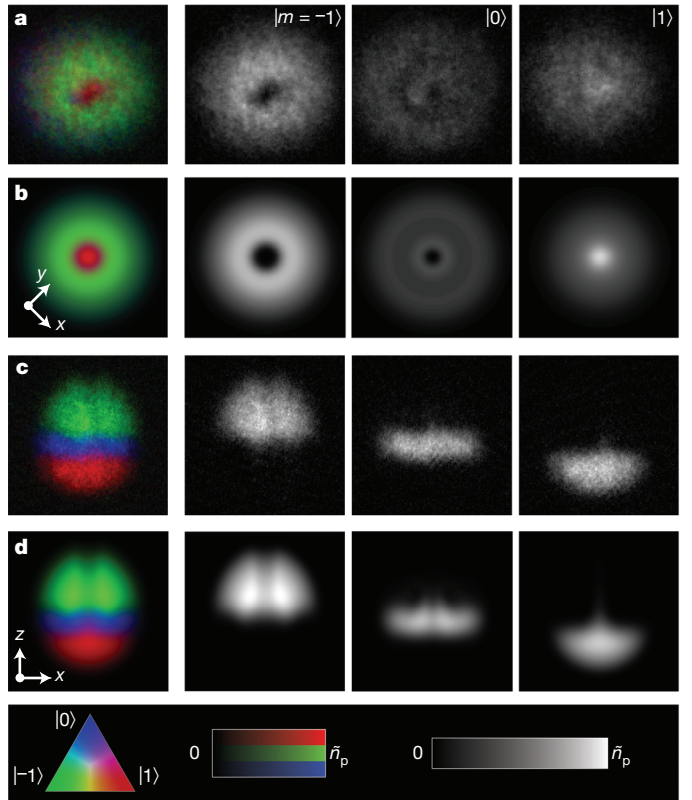
Figure 2 | Experimental creation of Dirac monopoles. Images of the condensate showing the integrated particle densities in different spin components as $B_{z,f}$ is decreased. Each row **a**–**f** contains images of an individual condensate. The leftmost column shows colour composite images of the column densities taken along the horizontal axis for the three spin states $\{|1\rangle, |0\rangle, |-1\rangle\}$; the colour map is given in **f**. Yellow arrows indicate the location of the nodal lines. The rightmost three columns show images taken along the vertical axis. The scale is 285 μm × 285 μm (horizontal) and 220 μm × 220 μm (vertical), and the peak column density is $\tilde{n}_p = 1.0 \times 10^9\ \text{cm}^{-2}$.

Figure 3 | Comparison between experiment and simulation. Experimental (**a**, **c**) and simulated (**b**, **d**) condensate particle densities with the monopole near the centre of the condensate. Comparisons along the vertical axis are shown in rows **a** and **b**, and those along the horizontal axis are shown in rows **c** and **d**. The hole observed in the $|-1\rangle$ component (row **a**) is discernible as a line of diminished density in row **c**. The field of view is 220 μm × 220 μm in **a** and **b** and 285 μm × 285 μm in **c** and **d**. The colour composite images and $\tilde{n}_p$ are as in Fig. 2.

numerical simulations (Fig. 4). We analyse these findings and discuss their implications below.

The spinor order parameter corresponding to the Dirac monopole[14,17] is generated by an adiabatic spin rotation in response to a time-varying magnetic field, $B(r, t)$. Similar spin rotations have been used to create multiply quantized vortices[18] and skyrmion spin textures[19]. The order parameter $\Psi(r, t) = \psi(r, t)\zeta(r, t)$ is the product of a scalar order parameter, ψ, and a spinor, $\zeta = (\zeta_{+1}, \zeta_0, \zeta_{-1})^T \cong |\zeta\rangle$, where $\zeta_m = \langle m | \zeta \rangle$ represents the mth spinor component along z. The condensate is initially spin-polarized along the z axis, that is, $\zeta = (1, 0, 0)^T$. Following the method introduced in ref. 14, a magnetic field $B(r,t) = b_q(x\hat{x} + y\hat{y} - 2z\hat{z}) + B_z(t)\hat{z}$ is applied, where $b_q > 0$ is the strength of a quadrupole field gradient and $B_z(t)$ is a uniform bias field. The magnetic field zero is initially located on the z axis at $z = B_z(0)/(2b_q) \gg Z$, where Z is the axial Thomas–Fermi radius of the condensate. The spin rotation occurs as B_z is reduced, drawing the magnetic field zero into the region occupied by the superfluid.

Ideally, the condensate spin adiabatically follows the local direction of the field (Fig. 1a–c). Our numerical analysis indicates, and both simulations and experiment confirm, that the fraction of atoms undergoing non-adiabatic spin-flip transitions is of order 1% for our experimental parameters. The spin texture in the adiabatic case is conveniently

expressed in a scaled and shifted coordinate system with $x' = x$, $y' = y$, $z' = 2z - B_z/b_q$, corresponding derivatives ∇', and spherical coordinates (r', θ', φ'). This transformation scales the z axis by a factor of two and shifts the origin of coordinates to coincide with the zero of the magnetic field. The applied magnetic field is then $B = b_q(x'\hat{x}' + y'\hat{y}' - z'\hat{z}')$. As B_z is reduced, each spin rotates by an angle $\pi - \theta'$ about an axis $\hat{n}(r', \theta', \varphi') = -\hat{x}' \sin \varphi' + \hat{y}' \cos \varphi'$. This spatially dependent rotation leads to a superfluid velocity

$$v_s = \frac{\hbar}{Mr'} \frac{1 + \cos \theta'}{\sin \theta'} \hat{\varphi}' \qquad (1)$$

and vorticity

$$\Omega = -\frac{\hbar}{Mr'^2}\hat{r}' + \frac{4\pi\hbar}{M}\delta(x')\delta(y')\Theta(z')\hat{r}' \qquad (2)$$

where M is the atomic mass, δ is the Dirac delta function and Θ is the Heaviside step function. The vorticity is that of a monopole attached to a semi-infinite vortex line singularity, of phase winding 4π, extending along the $+z'$ axis.

The synthetic vector potential arising from the spin rotation can be written as $A^* = -Mv_s/\hbar$, with the line singularity in A^* coincident with the nodal line in Ψ. However, this singularity is nonphysical, because it depends on the choice of gauge and can even be made to vanish[20] (Supplementary Information). The synthetic magnetic field of the monopole is therefore simply

$$B^* = \frac{\hbar}{r'^2}\hat{r}' \qquad (3)$$

The fields v_s and B^* are depicted in Fig. 1d.
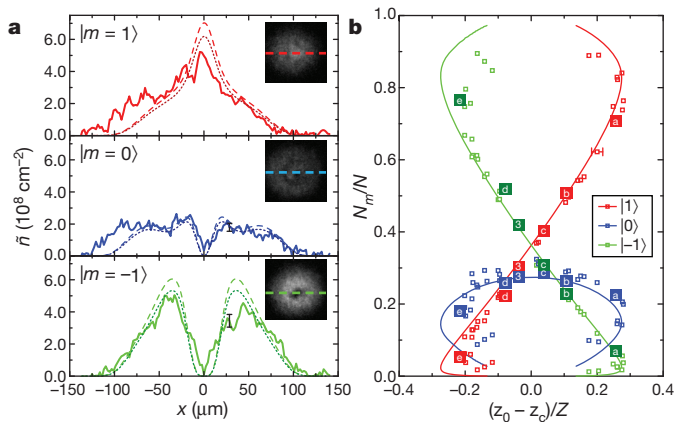
Figure 4 | Quantitative comparison between experiment and simulation.
a, Experimental (solid lines) and simulated (dashed and dotted lines) column densities $\bar{n}$ of the condensate from the vertical images in Fig. 3, with cross-sections taken as shown in the insets. Dotted lines show the approximate effect of three-body losses (see text). The origin $x = 0$ coincides with the hole in state $|0\rangle$. **b**, Fractions in each spin state for different positions of the centre of mass of the $|0\rangle$ state (z_0) relative to that of the condensate (z_c), in units of the axial Thomas–Fermi radius (Z). Solid lines are simulated values and points marked with letters and numbers correspond to panels **a**–**e** of Figs 2 and 3, respectively. Typical error bars that reflect uncertainties in the calibration of the imaging system are shown for several points.

The experimental set-up[21] is shown schematically in Fig. 1e. The optically trapped ^{87}Rb BEC consists of $N \approx 1.8(2) \times 10^5$ atoms in the $|F = 1, m = 1\rangle \equiv |1\rangle$ spin state, where the uncertainty reflects shot-to-shot variations and the calibration of the detection system. The calculated radial and axial Thomas–Fermi radii are $R = 6.5\,\mu\text{m}$ and $Z = 4.6\,\mu\text{m}$, respectively, and the corresponding optical trap frequencies are respectively $\omega_r \approx 2\pi \times 160\,\text{Hz}$ and $\omega_z \approx 2\pi \times 220\,\text{Hz}$. Four sets of coils are used to produce b_q, B_z and the transverse magnetic field components B_x and B_y, which are used to guide the applied magnetic field zero into the condensate. At the beginning of the monopole creation process, the bias field is $B_z = 10\,\text{mG}$. The quadrupole field gradient is then linearly ramped from zero to $b_q = 3.7\,\text{G}\,\text{cm}^{-1}$, placing the magnetic field zero approximately 30 μm above the condensate. The field zero is then brought down into the condensate by decreasing B_z linearly to $B_{z,f}$ at the rate $\dot{B}_z = -0.25\,\text{G}\,\text{s}^{-1}$. We call this the 'creation ramp'.

The atomic density of each spinor component $|m\rangle$ is imaged as established by the local spin rotation during the creation ramp (Methods). As the field zero passes through the condensate (Fig. 2a–f), the distribution of particles in the three spin states changes in a manner indicative of the expected spin rotation shown in Fig. 1. The nodal line appears in the images taken along the vertical axis as holes in the $|-1\rangle$ and $|0\rangle$ components, and in the side images as regions of reduced density extending vertically from the top of the condensate towards, but not through, the $|1\rangle$ component. This nodal line extends more deeply into the condensate as $B_{z,f}$ is reduced. Ultimately it splits into two vortex lines (Fig. 2f; see also Extended Data Fig. 1)—the characteristic signature of the decay of a doubly quantized vortex[22]—illustrating its 4π phase winding.

We compare the experimental images of the vertically (Fig. 3a) and horizontally (Fig. 3c) imaged density profiles with those given by numerical simulations (Fig. 3b, d) in which the monopole is near the centre of the condensate. The simulation data are obtained by solving the full three-dimensional dynamics of the spinor order parameter (Methods). The locations of the doubly quantized and singly quantized vortices in spinor components $|-1\rangle$ and $|0\rangle$ are visible in the experimentally acquired density profiles, as are other structures discernible in the images obtained from the numerical simulations. The observed vertical spatial separation of the spinor components (Fig. 3c) confirms that the vortex line terminates within the bulk of the condensate.

The quantitative agreement between experiment and simulation is apparent in Fig. 4, which shows cross-sections of the density profiles taken through the centre of the condensate. The differences observed in the peak densities (Fig. 4a) of the experimental (solid lines) and simulated (dashed lines) data are due to effects not taken into account in the simulation, such as three-body losses that were observed to be ~10% in the experiment. To show their effect, we have scaled the simulated data accordingly (dotted lines). Noting the absence of free parameters, the experimental data are in very good agreement with the numerical simulation.

We also show the fraction of the condensate in each spinor component for different vertical monopole locations within the condensate (Fig. 4b), including data from images in which the nodal line of the order parameter does not necessarily coincide with the z axis. The physical observable is the position of the centre of mass of the $|0\rangle$ component, z_0, relative to the centre of mass of the whole condensate, z_c. Again, we find that the experiments and simulations are in very good quantitative agreement without any free parameters.

An alternative description of the origins of the velocity and vorticity profiles (equations (1) and (2)) can be presented in terms of the motion of the monopole (Supplementary Information). As the monopole approaches the condensate, it is a source not only of the synthetic magnetic field, B^* (equation (3)), but also of an azimuthal synthetic electric field, E^*, described by Faraday's law, $\nabla' \times E^* = -\partial B^*/\partial t$. Each mass element of the superfluid is given a corresponding azimuthal acceleration by E^*. The monopole motion thereby induces the appropriate superfluid velocity and vorticity profiles within the condensate, in a manner similar to the induction of electric current in a superconducting loop by the motion of a (natural) magnetic monopole[23]. In our case, the condensate itself is the monopole detector, analogous to the superconducting loop. Being three-dimensional, however, it is sensitive to the entire 4π solid angle surrounding the monopole.

The creation and manipulation of a Dirac monopole in a controlled environment opens up a wide range of experimental and theoretical investigations. The time evolution and decay[14] of the monopole are of particular interest because it is not created in the ground state[24]. Interactions between the monopole and other topological excitations, such as vortices, present another fundamental research avenue with a variety of unexplored phenomena. There exists also the possibility of identifying and studying condensate spin textures that correspond to other exotic synthetic electromagnetic fields, such as that of the non-Abelian monopole[25]. Finally, the experimental methods developed in this work can also be directly used in the realization of a vortex pump[26], which paves the way for the study of peculiar many-body quantum states, such as those related to the quantum Hall effect[27].

Note added in proof: The effects of the Lorentz force arising from an inhomogeneous synthetic magnetic field have recently been observed in condensate dynamics[28].

METHODS SUMMARY

Imaging. After the creation ramp, we non-adiabatically change B_z from $B_{z,f}$ to a large value (typically several hundred milligauss) to project the condensate spinor components $\{|m\rangle\}$ into the approximate eigenstates of the Zeeman Hamiltonian while preserving the monopole spin texture. We call this the 'projection ramp'. The condensate is then released from the trap and allowed to expand for 22.9 ms. The three spin states are separated along the x axis during the expansion with a 3.5-ms pulse of the magnetic field gradient with the magnetic bias field pointing in the x direction. We take images simultaneously along the horizontal and vertical axes.
Data. The images shown in Figs 2 and 3 are selected from among several dozen similar images taken under identical conditions, and hundreds of similar images taken under similar conditions (see also Extended Data Fig. 2 for representative examples). Not every experimental run yields an image of a monopole, because drifts in the magnetic field and location of the optical trap cause the magnetic field zero to pass outside the BEC. Under optimal conditions, five to ten consecutive images may be taken before drifts require adjustment of the bias fields.
Simulation. We solve the full three-dimensional Gross–Pitaevskii equation with simulation parameters chosen to match those of the experiment, excepting the effects of three-body losses and the magnetic forces arising from the gradient

during the spin state separation just before imaging. To show the effects of the expansion, we present integrated particle densities of the condensate from the numerical simulation immediately after the creation ramp, and while the magnetic field zero is still in the condensate, in Extended Data Fig. 3. The volume considered varies from $20 \times 20 \times 20 a_r^3$ to $320 \times 320 \times 320 a_r^3$, where $a_r = \sqrt{\hbar/M\omega_r} \approx 0.9\ \mu m$ is the radial harmonic oscillator length. The size of the computational grid changes from $180 \times 180 \times 180$ to $1{,}024 \times 1{,}024 \times 1{,}024$ points.

Online Content Any additional Methods, Extended Data display items and Source Data are available in the online version of the paper; references unique to these sections appear only in the online paper.

1. Goldhaber, A. S. & Trower, W. P. (eds) *Magnetic Monopoles* (American Association of Physics Teachers, 1990).
2. Milton, K. A. Theoretical and experimental status of magnetic monopoles. *Rep. Prog. Phys.* **69,** 1637–1711 (2006).
3. Dirac, P. A. M. Quantised singularities in the electromagnetic field. *Proc. R. Soc. Lond. A* **133,** 60–72 (1931).
4. Vilenkin, A. & Shellard, E. P. S. (eds) *Cosmic Strings and Other Topological Defects* (Cambridge Univ. Press, 1994).
5. Castelnovo, C., Moessner, R. & Sondhi, S. L. Magnetic monopoles in spin ice. *Nature* **451,** 42–45 (2008).
6. Morris, D. J. P. *et al.* Dirac strings and magnetic monopoles in the spin ice $Dy_2Ti_2O_7$. *Science* **326,** 411–414 (2009).
7. Chuang, I., Durrer, R., Turok, N. & Yurke, B. Cosmology in the laboratory: defect dynamics in liquid crystals. *Science* **251,** 1336–1342 (1991).
8. Fang, Z. *et al.* The anomalous Hall effect and magnetic monopoles in momentum space. *Science* **302,** 92–95 (2003).
9. Milde, P. *et al.* Unwinding of a skyrmion lattice by magnetic monopoles. *Science* **340,** 1076–1080 (2013).
10. Blaha, S. Quantization rules for point singularities in superfluid ^{3}He and liquid crystals. *Phys. Rev. Lett.* **36,** 874–876 (1976).
11. Volovik, G. & Mineev, V. P. Vortices with free ends in superfluid He^3-A. *JETP Lett.* **23,** 647–649 (1976).
12. Salomaa, M. M. Monopoles in the rotating superfluid helium-3 A–B interface. *Nature* **326,** 367–370 (1987).
13. Volovik, G. *The Universe in a Helium Droplet* 214–217 (Oxford Univ. Press, 2003).
14. Pietilä, V. & Möttönen, M. Creation of Dirac monopoles in spinor Bose-Einstein condensates. *Phys. Rev. Lett.* **103,** 030401 (2009).
15. Lin, Y.-J., Compton, R. L., Jiménez-Garcia, K., Porto, J. V. & Spielman, I. B. Synthetic magnetic fields for ultracold neutral atoms. *Nature* **462,** 628–631 (2009).
16. Dalibard, J., Gerbier, F., Juzeliūnas, G. & Öhberg, P. Artificial gauge potentials for neutral atoms. *Rev. Mod. Phys.* **83,** 1523–1543 (2011).
17. Savage, C. M. & Ruostekoski, J. Dirac monopoles and dipoles in ferromagnetic spinor Bose-Einstein condensates. *Phys. Rev. A* **68,** 043604 (2003).
18. Leanhardt, A. E. *et al.* Imprinting vortices in a Bose-Einstein condensate using topological phases. *Phys. Rev. Lett.* **89,** 190403 (2002).
19. Choi, J.-y., Kwon, W. J. & Shin, Y.-i. Observation of topologically stable 2D skyrmions in an antiferromagnetic spinor Bose-Einstein condensate. *Phys. Rev. Lett.* **108,** 035301 (2012).
20. Wu, T. T. & Yang, C. N. Concept of nonintegrable phase factors and global formulation of gauge fields. *Phys. Rev. D* **12,** 3845–3857 (1975).
21. Kaufman, A. M. *et al.* Radio-frequency dressing of multiple Feshbach resonances. *Phys. Rev. A* **80,** 050701 (2009).
22. Shin, Y. *et al.* Dynamical instability of a doubly quantized vortex in a Bose-Einstein condensate. *Phys. Rev. Lett.* **93,** 160406 (2004).
23. Cabrera, B. First results from a superconductive detector for moving magnetic monopoles. *Phys. Rev. Lett.* **48,** 1378–1381 (1982).
24. Ruokokoski, E., Pietilä, V. & Möttönen, M. Ground-state Dirac monopole. *Phys. Rev. A* **84,** 063627 (2011).
25. Pietilä, V. & Möttönen, M. Non-Abelian magnetic monopole in a Bose-Einstein condensate. *Phys. Rev. Lett.* **102,** 080403 (2009).
26. Möttönen, M., Pietilä, V. & Virtanen, S. M. M. Vortex pump for dilute Bose-Einstein condensates. *Phys. Rev. Lett.* **99,** 250406 (2007).
27. Roncaglia, M., Rizzi, M. & Dalibard, J. From rotating atomic rings to quantum Hall states. *Sci. Rep.* **1,** 43 (2011).
28. Choi, J.-y. *et al.* Observation of a geometric Hall effect in a spinor Bose-Einstein condensate with a skyrmion spin texture. *Phys. Rev. Lett.* **111,** 245301 (2013).

METHODS

Condensate production. Condensates are produced in the $|F=2, m=2\rangle$ spin state of ^{87}Rb by sequential steps of evaporative cooling, first in a time-averaged, orbiting potential magnetic trap and subsequently in a 1,064-nm crossed-beam optical dipole trap. The two evaporation stages are used to avoid the introduction of vortices that occasionally arise during the transfer of a condensate from the magnetic trap to the optical trap. The radial and axial optical trap frequencies at the end of the evaporative cooling process are ~110 and ~130 Hz, respectively. A subsequent microwave Landau–Zener sweep drives the condensate into the $|F=1, m=1\rangle$ state.

After having established $B_z = 10$ mG, the trap frequencies are increased to $\omega_r \approx 2\pi \times 160$ Hz and $\omega_z \approx 2\pi \times 220$ Hz before the quadrupole field is turned on. The tighter trap better resists the magnetic forces exerted by the field gradient, but it also limits the condensate lifetime to approximately 500 ms as a result of three-body loss processes. At the end of the experiment, $N \approx 1.6 \times 10^5$, indicating typical three-body losses of ~10%.

Magnetic field control. The x, y and z axes are defined by the orientation of the magnetic field coils BX, BY and BZ, as shown in Fig. 1e. The magnetic fields are calibrated to within ~1 mG using Majorana spectroscopy, in which the field component along the z axis is rapidly (15 G s^{-1}) reversed and the fraction of atoms thereby transferred non-adiabatically to the $|-1\rangle$ state is measured as a function of the currents applied to the BX and BY field coils. Maximum transfer occurs when the transverse field components are minimized. The field along the z axis is similarly calibrated by rapidly reversing the field component along the x axis.

Precise magnetic field control at the location of the condensate is one of the most challenging aspects of the experiment. The condensate presents a small target (~7 µm) into which the field zero must be guided. The creation process is therefore quite sensitive to drifts in the relative position of the optical trap and the position of the field zero, limiting our ability to generate large sequential data sets without compensatory adjustments. Such drifts may be caused either by fluctuating background fields or by mechanical instabilities in the trapping beam optics. With $b_q = 3.7$ G cm^{-1}, a 1-mG change in the radial field corresponds to a translation of the zero by 1.4 µm, or 25% of the condensate radius—enough to disturb the creation of the monopole. Similar shifts alter the vertical bias field required to bring the field zero into the condensate.

An additional complication is that the centre of the optical trap and the physical centre of the gradient coils do not in general coincide, and can drift with respect to one another. Relative to the centre of the gradient coils, the condensate can be offset horizontally by as much as 14 µm, and downwards by as much as ~25 µm.

Adiabatic spin rotation. As B_z changes during the monopole creation process, the condensate spin ideally remains in the strong-field seeking state (SFSS), that is, the minimum-energy eigenstate of the local Zeeman Hamiltonian. At the field zero, however, the local Zeeman term of the Hamiltonian vanishes and non-adiabatic spin transitions to the neutral and weak-field seeking states become inevitable. Neglecting the kinetic energy related to spin rotations and the weak spin–spin interactions in the condensate, the spatially dependent probability of successful adiabatic spin rotation when the homogeneous bias field is inverted from large positive values to large negative values can be approximated within the three-level Landau–Zener model by[29]

$$\Pi_{ad}(x,y) = \left\{ 1 - \exp\left[\frac{\pi \mu_B b_q^2 (x^2+y^2)}{4\hbar |\dot{B}_z|} \right] \right\}^2 \tag{4}$$

where μ_B is the Bohr magneton. The fraction of particles remaining in the SFSS can be approximated by an average of equation (4) weighted by a fixed particle density, $\bar{n}(r)$, as

$$P_{ad} = \frac{\int \bar{n}(r) \Pi_{ad}(r) d^3 r}{\int \bar{n}(r) d^3 r} \tag{5}$$

Applying equations (4) and (5) to the initial vortex-free density distribution determined by solving the Gross–Pitaevskii equation with the parameter values extracted from the experiments, we obtain $P_{ad} = 98\%$. The doubly quantized vortex generated during the field inversion reduces the number of atoms in precisely the region where the undesired spin flips are most probable. For a density distribution that includes the doubly quantized vortex along the z axis, equations (4) and (5) yield $P_{ad} = 99\%$. Full numerical simulations of the creation of the doubly quantized vortex confirm that 99% of the particles remain in the SFSS.

Experimentally, P_{ad} is controlled by b_q and $\dot{B}_z$. Increasing b_q results in stronger magnetic forces on the condensate due to the gradient, which must remain small relative to those exerted by the optical trap so as not to perturb the condensate position extensively. The strength of the optical trap, however, cannot itself be increased without compromising both the size of the condensate and its lifetime. Choosing $b_q = 3.7$ G cm^{-1} was found convenient in this respect.

Decreasing $\dot{B}_z$, on the other hand, results in lengthier exposures of the BEC to magnetic field noise that can possibly induce undesirable spin transitions. The noise associated with the power mains (at frequencies that are odd-integer (n) multiples of 60 Hz) is the most serious, being resonant at a field of $n \times 85$ µG. The choice $\dot{B}_z = -0.25$ G s^{-1} ensures that the resonance condition is passed in less time than a single oscillation period of the noise, at least up to $n = 7$. The effect of this noise is merely to distort slightly the path traced by the field zero during the creation ramp.

With the experimental parameters described above, we find that a negligible number of atoms are excited out of the SFSS after the field zero is moved fully through the condensate. Only when we increase the ramp rates by an order of magnitude do we find a discernible fraction of the atoms in the weak-field seeking state. This is consistent with the simulations and the calculation of P_{ad}. We conclude that non-adiabatic spin flips are not important in the monopole creation process with the parameters used in the experiments, and that the Landau–Zener model describes this phenomenon well.

Imaging. At the end of the creation ramp, B_z is rapidly decreased (in 0.040 ms) until $|B_z/B_{z,f}| \gg 1$, a stage we call the 'projection ramp'. This non-adiabatic field ramp keeps the order parameter essentially unchanged but takes the spin states $\{|m\rangle\}$ to be the approximate eigenstates of the Zeeman Hamiltonian. As described below, we image the particle density in each of these new eigenstates, accessing the detailed structure of the monopole established by the creation ramp.

Immediately after the projection ramp, the magnetic field gradient is turned off in 0.350 ms. The optical trapping beams are then extinguished, releasing the condensate from the trap and permitting it to expand freely for 4 ms. The field is then increased adiabatically (in 1 ms) to 13.7 G in the x direction as B_z is simultaneously reduced to zero. After a 1.5-ms delay, the magnetic gradient coils are pulsed on for 3.5 ms to 20.1 G cm^{-1} (radial) to separate the spin states horizontally.

The total time of flight of the atoms is 22.9 ms, counted from the moment of release from the optical trap. After expansion, the condensates are imaged absorptively along both the vertical (z) and horizontal (y) axes simultaneously (to within 14 µs) in the presence of a 0.1-G imaging field directed along z. In the absorption images, we correct for neither the slightly different sensitivities of the different spin states to the probe beam nor the slightly different expansions that result from the applied magnetic field gradient.

Although we describe in this paper the creation of the monopole with the initial parameters $b_q > 0$, $B_z(t=0) > 0$ and $\dot{B}_z < 0$, the process yields essentially identical results experimentally when $b_q > 0$, $B_z(t=0) < 0$ and $\dot{B}_z > 0$ in the creation ramp, except that the field zero enters the condensate along the negative z axis and thereby changes the sense of the spin rotation. Similarly, B_z can be rapidly increased in either the $+z$ or the $-z$ direction in the projection ramp with the same outcomes (Extended Data Fig. 2).

The images shown in Figs 2 and 3 are selected from among dozens of similar images taken under identical conditions, and hundreds of images taken under similar conditions (Extended Data Fig. 2). Not every image demonstrates the signature presence of a monopole, because drifts in the magnetic fields and the location of the optical trap eventually cause the magnetic field zero to miss the condensate. Under optimal conditions, we find that we can take five to ten sequential images in which the field zero passes through the condensate, after which we must adjust the magnetic bias fields to re-centre the magnetic field zero on the condensate.

The first images of pairs of singly quantized vortices that indicate the passage of the monopole through the condensate were taken on 6 February 2013. Consistent images of the condensate density distributions associated with the monopole were first obtained on 1 March 2013.

Numerical simulation. The experimental set-up is simulated by solving the full three-dimensional Gross–Pitaevskii equation. The simulation parameters are chosen to match those of the experiment, but we include neither the effects of three-body losses nor the magnetic forces arising from the gradient during the spin state separation just before imaging. The particle number is held fixed at $N = 1.8 \times 10^5$, corresponding to the initial number of atoms in the experiment. We can roughly account for the three-body losses by scaling the obtained particle density by the fraction of atoms that remain at the end of the experiment. Otherwise, the simulations are performed with the time-dependent parameters identical to those used in the experiment.

The volume considered varies from $20 \times 20 \times 20 a_r^3$ to $320 \times 320 \times 320 a_r^3$, where $a_r = \sqrt{\hbar/M\omega_r} \approx 0.9$ µm is the radial harmonic oscillator length. The size of the computational grid changes from $180 \times 180 \times 180$ to $1,024 \times 1,024 \times 1,024$ points. The initial spin-polarized state is obtained with a relaxation method and the temporal evolution is computed using a split-operator technique employing Fourier transforms for the kinetic energy part. The time required for the computation is reduced with the help of graphics processing units, coordinate transformations and an adaptive computational grid.

Effects of free expansion. The condensate must be allowed to expand freely to image its spin structure and determine the presence of the monopole. The condensate is therefore not imaged while the magnetic field zero is within the condensate. To demonstrate the effects of the free expansion on the spin structure, we show the simulated particle densities of the condensate just after the creation ramp in Extended Data Fig. 3. The images are created from an intermediate step in the complete simulation that is used to produce Fig. 2. The principal effects of the release of the condensate are its expansion with different speeds in different directions, the increase in the relative vortex core sizes, the partial filling of the vortex cores with other spinor components, and the slight separation of the different spinor components. The last three effects are due exclusively to the repulsive interactions between the atoms during the first few milliseconds of expansion. Because there is excellent agreement between the simulated and experimentally observed results in Fig. 3, we conclude that Extended Data Fig. 3 is a suitable representation of the condensate just after the creation ramp, while the field zero is still within the superfluid.

29. Carroll, G. E. & Hioe, F. T. Further generalization of Landau-Zener calculation. *J. Opt. Soc. Am. B* **2,** 1355–1360 (1985).
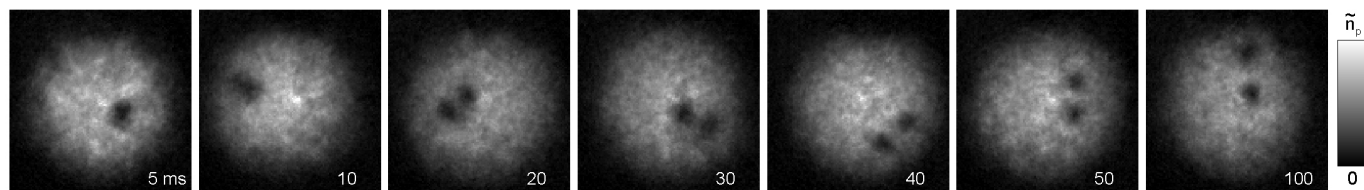
Extended Data Figure 1 | Decay of the doubly quantized vortex. Images of the condensate time evolution after moving the magnetic field zero completely through the condensate. The evolution time is shown at the bottom right of each panel. The maximum pixel intensity corresponds to a peak column density $\tilde{n}_p = 1.0 \times 10^9$ cm^{-2}, and the field of view is 246 μm × 246 μm. Each image represents a separate condensate, and $\dot{B}_z = 3$ G s^{-1}. After roughly 10 ms the vortex splits in two, demonstrating the initial 4π phase winding of the nodal line.
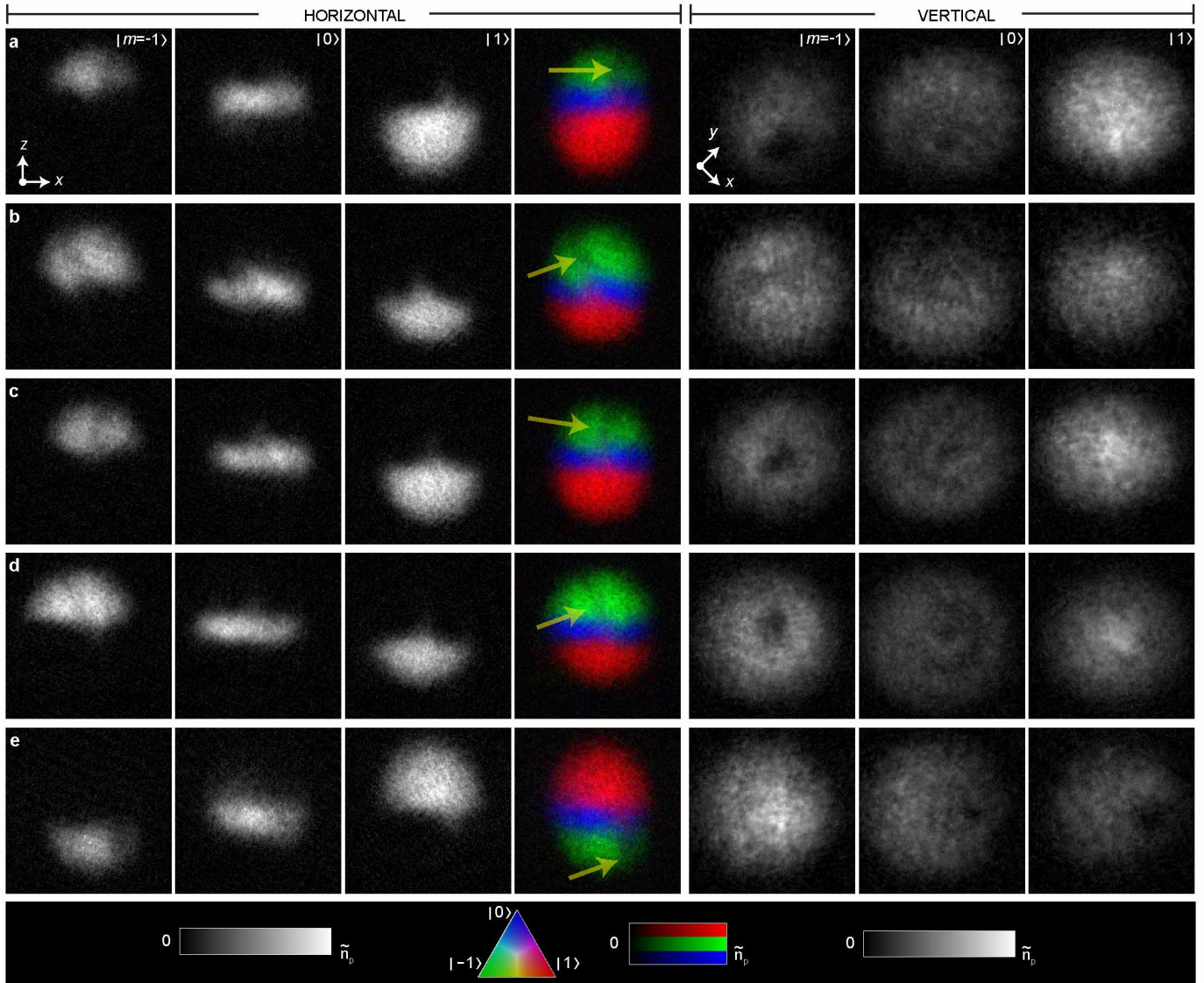
Extended Data Figure 2 | Additional representative images of Dirac monopoles. Each row contains images of the same condensate. The maximum pixel intensity corresponds to $\tilde{n}_p = 8.2 \times 10^8$ cm^{-2}, and the field of view is 220 μm × 220 μm in the vertical images and 285 μm × 285 μm in the horizontal images. The arrow points to the density depletion that is identified as the nodal line. In **a**–**c**, we use the same protocol outlined in the paper: an off-centre monopole (**a**); an angled nodal line that is visible in the side image but not in the vertically directed image (**b**); and a nodal line that appears to be splitting into two vortices in the $|m = -1\rangle$ component (**c**). **d**, An example of a monopole spin structure in which the creation ramp is as described in the text but the projection ramp is reversed (that is, B_z is rapidly increased until $|B_z/B_{z,f}| \gg 1$). **e**, Monopole spin structure created by moving the field zero into the condensate from below with $\dot{B}_z > 0$. The projection ramp is performed as described in **d**.
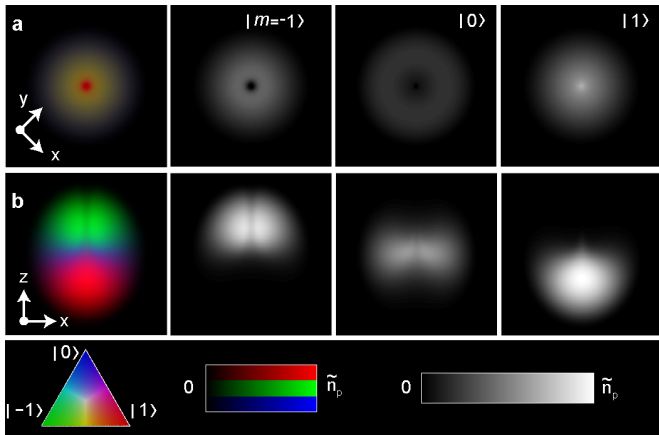
Extended Data Figure 3 | Numerical simulation of integrated particle densities before expansion. Vertically (**a**) and horizontally (**b**) integrated particle densities of a condensate just before the projection ramp, with $B_{z,f}$ chosen such that the monopole is in the centre of the condensate. The fields of view are 17.2 μm × 17.2 μm (**a**) and 17.2 μm × 11.4 μm (**b**); in **b,** it is reduced in the z direction for a more convenient comparison with the simulations shown in Fig. 3. The maximum pixel intensity corresponds to $\tilde{n}_p = 2.98 \times 10^{11}$ cm^{-2}.